Evidence of an odd-parity hidden order in a spin–orbit coupled correlated iridate

L. Zhao[1,2], D. H. Torchinsky[1,2], H. Chu[2,3], V. Ivanov[1], R. Lifshitz [1,4], R. Flint[5], T. Qi[6], G. Cao[6] and D. Hsieh[1,2]*

A rare combination of strong spin–orbit coupling and electron–electron correlations makes the iridate Mott insulator Sr_2IrO_4 a promising host for novel electronic phases of matter[1,2]. The resemblance of its crystallographic, magnetic and electronic structures[1-6] to La_2CuO_4, as well as the emergence on doping of a pseudogap region[7-9] and a low-temperature d-wave gap[10,11], has particularly strengthened analogies to cuprate high-T_c superconductors[12]. However, unlike the cuprate phase diagram, which features a plethora of broken symmetry phases[13] in a pseudogap region that includes charge density wave, stripe, nematic and possibly intra-unit-cell loop-current orders, no broken symmetry phases proximate to the parent antiferromagnetic Mott insulating phase in Sr_2IrO_4 have been observed so far, making the comparison of iridate to cuprate phenomenology incomplete. Using optical second-harmonic generation, we report evidence of a hidden non-dipolar magnetic order in Sr_2IrO_4 that breaks both the spatial inversion and rotational symmetries of the underlying tetragonal lattice. Four distinct domain types corresponding to discrete 90°-rotated orientations of a pseudovector order parameter are identified using nonlinear optical microscopy, which is expected from an electronic phase that possesses the symmetries of a magneto-electric loop-current order[14-18]. The onset temperature of this phase is monotonically suppressed with bulk hole doping, albeit much more weakly than the Néel temperature, revealing an extended region of the phase diagram with purely hidden order. Driving this hidden phase to its quantum critical point may be a path to realizing superconductivity in Sr_2IrO_4.

The crystal structure of the $5d$ transition metal oxide Sr_2IrO_4 is tetragonal and centrosymmetric with four-fold (C_4) rotational symmetry about the c-axis[2-6]. It is composed of stacked IrO_2 square lattices whose unit cell is doubled relative to the CuO_2 square lattices found in high-T_c cuprates as a result of a staggered rotation of the octahedral oxygen cages (Fig. 1a). Despite the much larger spatial extent of $5d$ versus $3d$ orbitals, Sr_2IrO_4 is a Mott insulator by virtue of strong atomic spin–orbit coupling[1,2]. The electronic states near the Fermi level derive predominantly from the t_{2g} d-orbitals of iridium ions, which are well approximated as two completely filled spin–orbital entangled $J_{eff} = 3/2$ bands and one half-filled $J_{eff} = 1/2$ band, which is split into an upper and lower Hubbard band by an on-site Coulomb interaction. Below a Néel temperature $T_N \sim 230$ K, the spin–orbital entangled $J_{eff} = 1/2$ magnetic dipole moments undergo three-dimensional long-range ordering into an orthorhombic antiferromagnetic structure[2-5] that preserves global inversion symmetry but lowers the rotational symmetry of the system from C_4 to C_2. No additional symmetry breaking has otherwise been observed by neutron or X-ray diffraction.

Optical second-harmonic generation (SHG), a frequency doubling of light through its nonlinear interaction with a material, is strongly affected by point group symmetry changes[19] and can be used to search for hidden phases with higher-rank tensor order parameters that are difficult to detect using conventional probes[18,20]. It is particularly sensitive to inversion symmetry breaking because the leading-order electric-dipole (ED) contribution to SHG, which is described by a third-rank susceptibility tensor χ_{ijk}^{ED} that relates the nonlinear polarization at the second-harmonic frequency 2ω to the incident electric field via $P_i(2\omega) \propto \chi_{ijk}^{ED} E_j(\omega) E_k(\omega)$, is allowed only if the crystal lacks an inversion centre. Otherwise SHG can arise only from much weaker higher-rank multipole processes, as is the case for the Sr_2IrO_4 crystal structure described below. The rotational symmetry of a crystal can be directly determined by performing a rotational anisotropy (RA) SHG experiment where the intensity of obliquely reflected SHG is measured as a function of the angle φ through which the scattering plane is rotated about the surface normal of the crystal (Fig. 1b). For our experiment, the incident light is focused onto optically flat regions of the crystal surface with a spot size $d < 100\,\mu m$. The polarizations of the incident (in) and reflected (out) beams can be independently selected to be either parallel (P) or perpendicular (S) to the scattering plane, thus allowing different nonlinear susceptibility tensor elements to be probed.

Figure 1c shows room-temperature RA-SHG patterns of Sr_2IrO_4 measured by rotating the scattering plane about its c-axis. The data measured under both $P_{in}–P_{out}$ and $P_{in}–S_{out}$ polarization geometries (see Supplementary Section 1 for other geometries) exhibit a clear C_4 symmetry and are completely accounted for by the leading-order non-local bulk contribution to SHG of electric-quadrupole (EQ) type[6], which can be written as an effective nonlinear polarization $P_i(2\omega) \propto \chi_{ijkl}^{EQ} E_j(\omega) \nabla_k E_l(\omega)$. No surface ED contribution to SHG was detected within our instrument sensitivity[6]. As discussed in ref. 6, the rotation of the SHG intensity maxima away from the crystallographic a and b axes and their modulated amplitude in the $P_{in}–S_{out}$ pattern clearly signify the absence of mirror symmetry across the a–c and b–c planes. Expressions for the RA-SHG patterns (Supplementary Section 2) calculated using the set of independent non-vanishing tensor elements of the fourth-rank susceptibility tensor χ_{ijkl}^{EQ} derived from the experimentally

[1]Department of Physics, California Institute of Technology, Pasadena, California 91125, USA. [2]Institute for Quantum Information and Matter, California Institute of Technology, Pasadena, California 91125, USA. [3]Department of Applied Physics, California Institute of Technology, Pasadena, California 91125, USA. [4]Raymond and Beverly Sackler School of Physics and Astronomy, Tel Aviv University, Tel Aviv 69978, Israel. [5]Department of Physics and Astronomy, Iowa State University, Ames, Iowa 50011, USA. [6]Center for Advanced Materials, Department of Physics and Astronomy, University of Kentucky, Lexington, Kentucky 40506, USA. *e-mail: dhsieh@caltech.edu
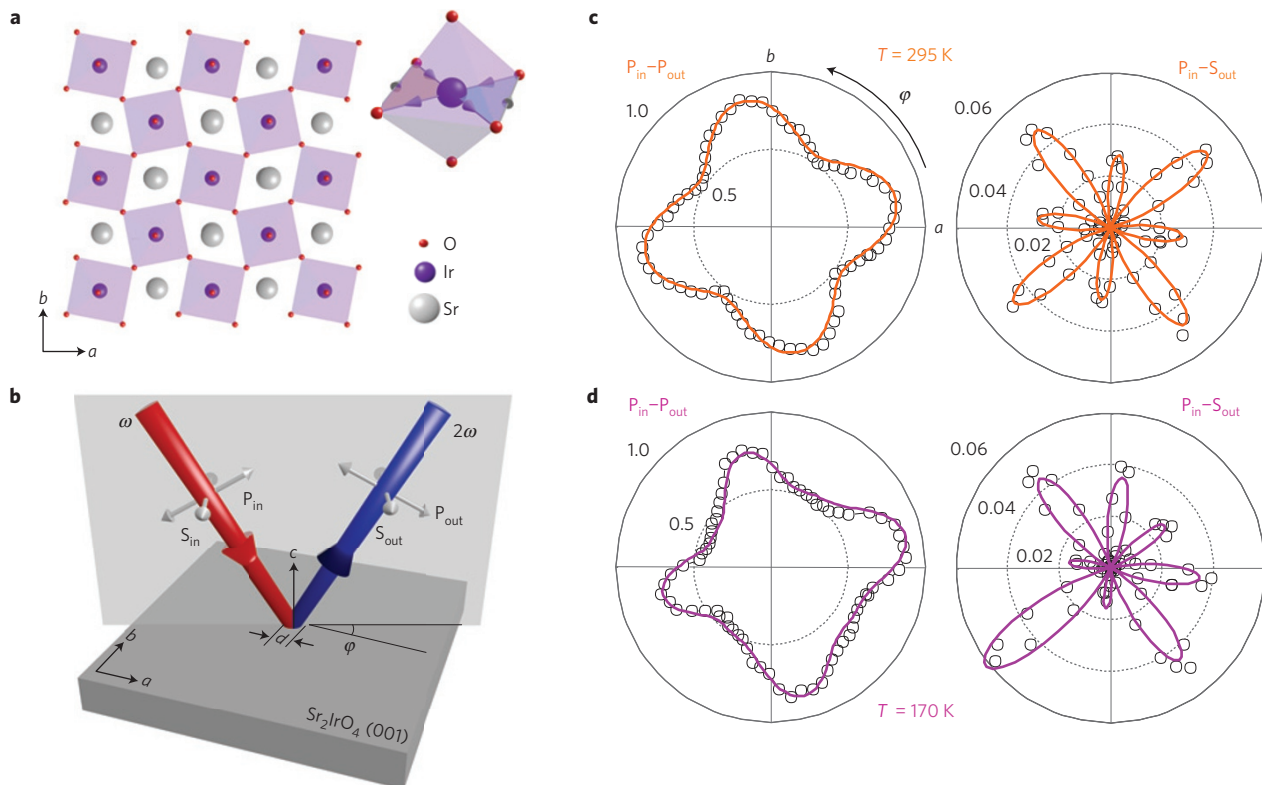
Figure 1 | Symmetry of the hidden order in Sr_2IrO_4. a, Crystal structure of a single perovskite layer in Sr_2IrO_4 (tetragonal point group $4/m$). Inset shows the basic IrO_6 unit of the magneto-electric loop-current order, with the arrows pointing in the direction of current flow. **b**, Schematic of the RA-SHG experiment. The electric field polarizations of the obliquely incident fundamental beam (in) and outgoing SHG beam (out) can be independently selected to lie either parallel (P) or perpendicular (S) to the light scattering plane (shaded). RA-SHG data are acquired by measuring the SHG intensity $I(2\omega)$ reflected from the (001) surface of Sr_2IrO_4 as a function of the angle φ between the scattering plane and crystal a–c-plane. **c**, RA-SHG data collected under P_{in}–P_{out} and P_{in}–S_{out} polarization geometries using $\lambda = 800$ nm incident light at $T = 295$ K. **d**, Analogous data to **c** collected at $T = 170$ K. All data sets are plotted on the same intensity scale, normalized to a value of 1, which corresponds to ~20 fW. The high-temperature data are fitted to time-reversal invariant bulk electric-quadrupole-induced SHG (orange lines). The low-temperature data can only be fitted to the coherent sum of time-reversal invariant bulk electric-quadrupole-induced and time-reversal broken bulk electric-dipole-induced SHG (purple lines), as described in the text.

established centrosymmetric $4/m$ crystallographic point group of Sr_2IrO_4 fit the data extremely well (Fig. 1c).

Remarkably, the rotational symmetry of the RA-SHG patterns measured at low temperature ($T = 170$ K) is reduced from C_4 to C_1 (Fig. 1d). This is not caused by a structural distortion because extensive neutron and resonant X-ray diffraction studies show no change in crystallographic symmetry below room temperature[2–5]. It cannot be accounted for by the antiferromagnetic structure that develops below $T_N \sim 230$ K because that has a centrosymmetric orthorhombic magnetic point group ($2/m1'$) with C_2 symmetry (Supplementary Section 3). Ferro- or antiferroelectric order can also be ruled out owing to the absence of any anomaly in the temperature dependence of the dielectric constant of Sr_2IrO_4 above $T = 170$ K (ref. 21). Instead, the ordering of a higher multipolar degree of freedom that coexists with the $J_{eff} = 1/2$ moment in each IrO_6 octahedron is left as the most plausible explanation. An ordering of higher-rank parity-even magnetic multipoles with the same propagation wavevector as the antiferromagnetic structure has, in fact, been proposed to occur in Sr_2IrO_4 below T_N (refs 22,23). Such an order would naturally be difficult to detect using diffraction-based probes because it preserves the translational symmetry of the antiferromagnetic lattice and imparts no net magnetization to the crystal.

To investigate this possibility, we surveyed all magnetic subgroups of the crystallographic $4/m$ point group of Sr_2IrO_4 that do not include the two-fold rotation axis (2) as a group element. We find that our data are uniquely but equally well described by

two subgroups ($2'/m$ and $m1'$) of the antiferromagnetic point group. Both $2'/m$ and $m1'$ break the global inversion symmetry of the crystal and thus allow a bulk ED contribution to SHG on top of the existing EQ contribution, which is consistent with the large changes observed in the SHG amplitude. Moreover, expressions for the RA-SHG pattern calculated using a coherent sum of the crystallographic EQ and the hidden-order-induced ED contributions (Supplementary Section 2), with the elements of χ_{ijkl}^{EQ} derived from a $4/m$ point group and those of χ_{ijk}^{ED} derived from either a $2'/m$ or $m1'$ point group, fit the data extremely well (Fig. 1d). However this indicates that an ordering of higher-rank parity-even magnetic multipoles, which preserves global inversion symmetry, cannot be the origin of our RA-SHG results.
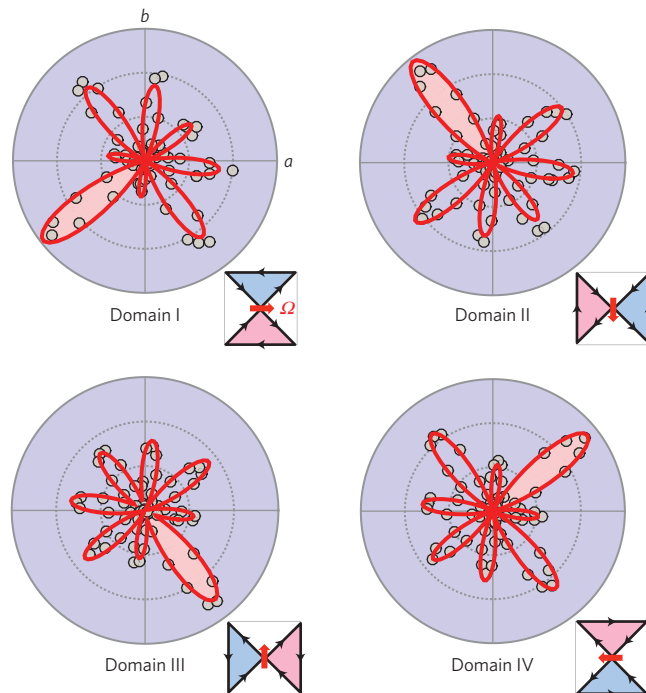
On the other hand, our results can be explained by an ordering of higher-rank parity-odd magnetic multipoles that preserves the translational symmetry of either the antiferromagnetic structure or the crystallographic structure. A microscopic model that satisfies this condition as well as the $2'/m$ or $m1'$ point group symmetries is the magneto-electric loop-current order (Supplementary Section 4), which is predicted to exist in the pseudogap region of the cuprates[14–18,20] but can in principle persist even at half-filling[24]. This phase consists of a pair of counter-circulating current loops in each CuO_2 square plaquette (Fig. 1a inset) and can be described by a toroidal pseudovector[25,26] order parameter defined as $\Omega = \Sigma \mathbf{r}_i \times \mathbf{m}_i$, where $\mathbf{r}_i$ is the location of the orbital magnetic moment $\mathbf{m}_i$ inside the plaquette. Four degenerate configurations are possible because the two intra-unit-cell current loops can lie along either of two diagonals
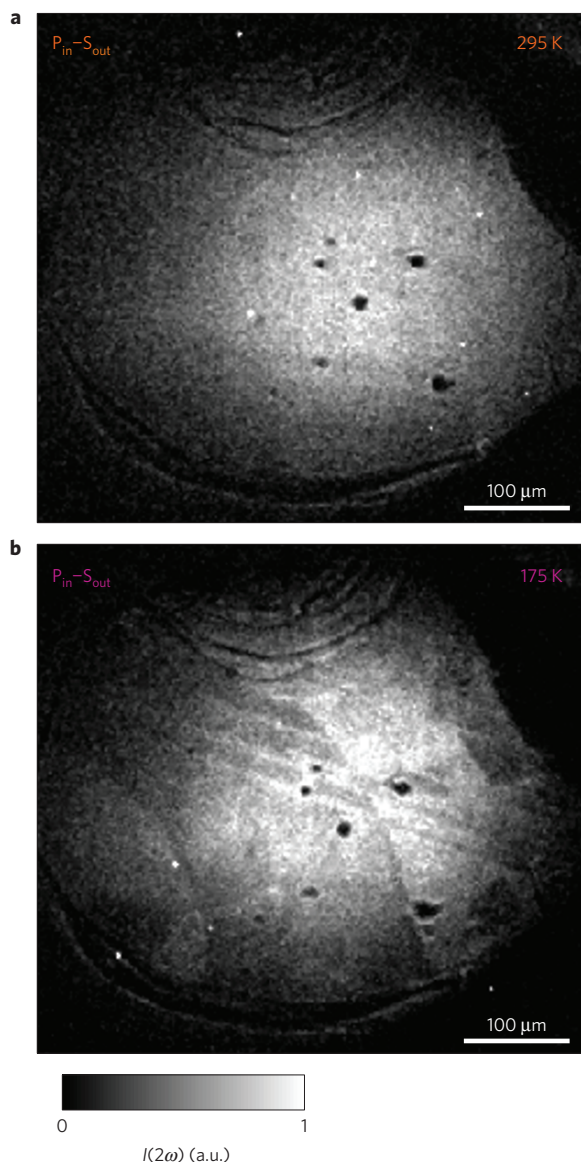
Figure 2 | Spatial mapping of hidden order domains. a,b, Wide-field reflection SHG microscopy images of the cleaved (001) plane of Sr_2IrO_4 measured under P_{in}–S_{out} polarization geometry at $\varphi = 78°$ at $T = 295$ K (**a**) and at $T = 175$ K (**b**). A patchwork of light and dark regions present in the low-temperature image arises from domains of the hidden order. The dark curves at the sample edge and dark micrometre-sized spots near the sample centre that are visible in both the high- and low-temperature images are structural defects.

**Figure 3 | Degenerate ground-state configurations of the hidden order.** Four different types of RA-SHG patterns found by performing local measurements within all of the domains mapped in Fig. 2b. Red lines are fits to the expressions described in the text. The large lobes are shaded pink to emphasize the orientation of each pattern. Schematics of the four degenerate magneto-electric loop-current order configurations are shown below each pattern to illustrate the possible correspondence. The red arrows denote the direction of the toroidal moment Ω in each plaquette.

in the square plaquette and can have either of two time-reversed configurations, which correspond to four 90°-rotated directions of the pseudovector. In a real material, one therefore expects domains of all four types to be populated.

To search for domains of the hidden order in Sr_2IrO_4 we performed wide-field reflection SHG microscopy measurements. A room-temperature P_{in}–S_{out} SHG image collected on a clean ~500 μm × 500 μm region parallel to the a–b plane is shown in Fig. 2a. This region produces a uniform SHG response consistent with the behaviour of a single crystallographic domain. On cooling to $T = 175$ K, brighter and darker patches separated by boundaries that are straight over a length scale of tens of micrometres become visible (Fig. 2b). The distribution and shapes of these patches can be rearranged on thermal cycling (Supplementary Section 5),

which suggests that they are not pinned to structural defects in the crystal. To examine whether the different patches observed in Fig. 2b correspond to domains with different Ω orientation, we performed local RA-SHG measurements within each of the patches. An exhaustive study over the entire crystal area in Fig. 2b reveals a total of only four types of patches, characterized by the four distinct RA-SHG patterns (Supplementary Section 6) shown in Fig. 3, which are exactly 0°-, 90°-, 180°- and 270°-rotated copies of those shown in Fig. 1. These results are consistent with the hidden phase in Sr_2IrO_4 being a magneto-electric loop-current order—but other microscopic models that obey the same set of symmetries certainly cannot be ruled out.

The ordering temperature T_Ω of the hidden phase in Sr_2IrO_4 was determined by measuring the temperature dependence of the SHG intensity in the P_{in}–S_{out} polarization geometry where the hidden-order-induced changes are largest. The onset of change is clearly observed at $T_\Omega \sim 232$ K, as shown in Fig. 4a, which is close to but slightly higher than the value of $T_N \sim 230$ K determined by d.c. magnetic susceptibility measurements, and evolves with an order-parameter-like behaviour on further cooling (Supplementary Section 7). In a Landau free energy expansion (Supplementary Section 8), a bilinear coupling between the antiferromagnetic Néel and hidden order parameters is forbidden by symmetry, so there is no a priori reason that T_Ω and T_N should coincide. The close proximity of T_Ω and T_N observed in Sr_2IrO_4 therefore suggests some microscopic mechanism by which one order can induce the other through a biquadratic coupling—an enhancement of the super-exchange coupling between $J_{eff} = 1/2$ moments due to the presence of hidden order being one possible scenario.

To experimentally examine whether or not the Néel and hidden orders are trivially tied, we performed analogous SHG experiments
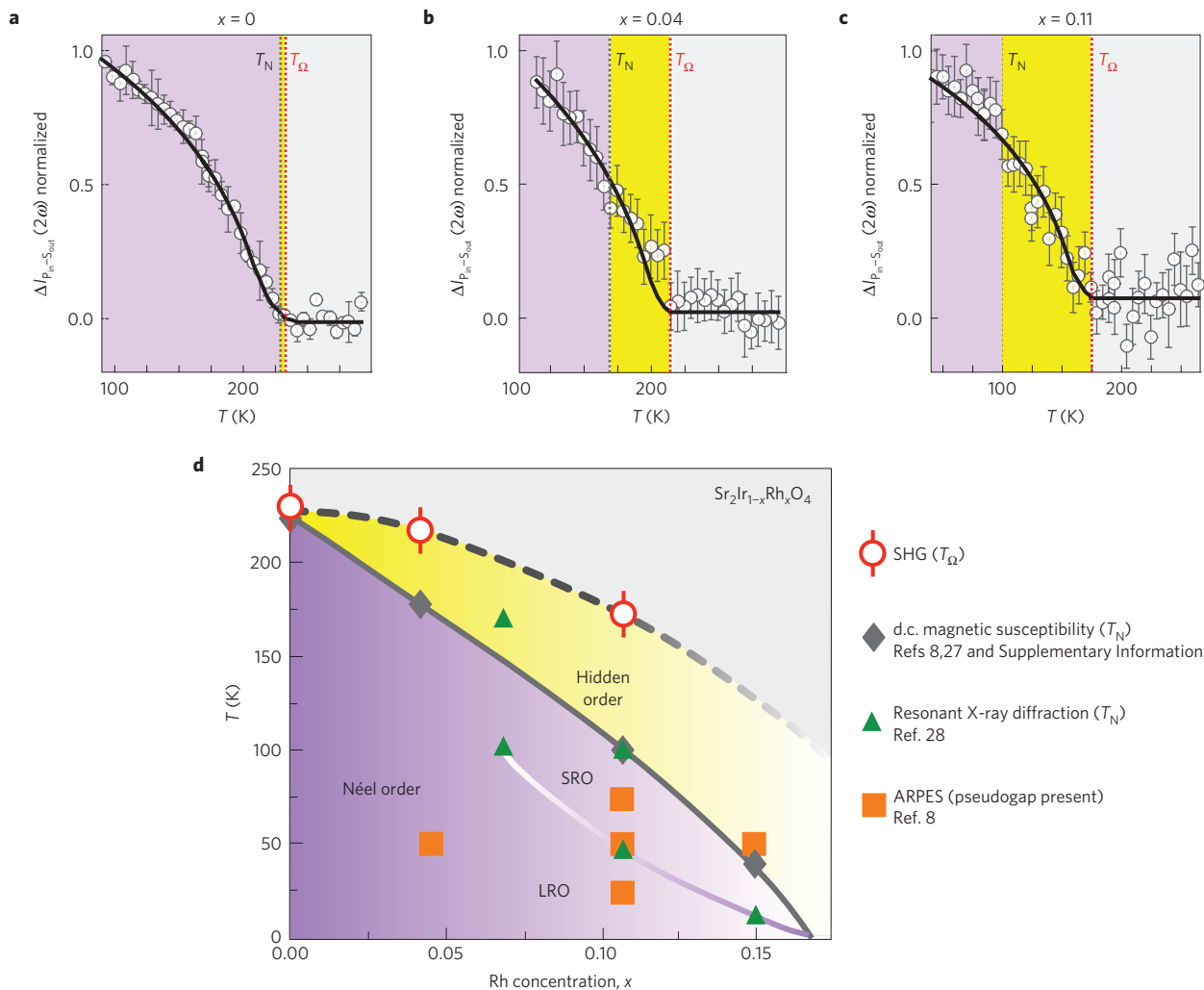
Figure 4 | Temperature and hole-doping dependence of the hidden order. a-c, Change in SHG intensity from $Sr_2Ir_{1-x}Rh_xO_4$ at $x=0$ (**a**), $x=0.04$ (**b**) and $x=0.11$ (**c**) measured relative to their room-temperature values as a function of temperature. Data were taken under $P_{in}-S_{out}$ polarization geometry at $\varphi=78°$. The error bars represent the standard deviation over 60 independent measurements. No difference was observed between curves measured on cooling and heating. Lines are guides to the eye. The dashed red lines mark the transition temperature T_Ω of the hidden order phase deduced from our SHG data and the dashed black lines mark the Néel temperature T_N determined from d.c. magnetic susceptibility measurements. **d**, Temperature versus doping phase diagram of $Sr_2Ir_{1-x}Rh_xO_4$ showing the boundaries of the hidden order and the long-range (LRO) and short-range (SRO) Néel ordered regions. Points where a pseudogap is present are also marked, although a pseudogap phase boundary is not yet experimentally known.

on hole-doped $Sr_2Ir_{1-x}Rh_xO_4$ crystals (Supplementary Section 9) to track the evolution of T_Ω as a function of Rh concentration (x). Bulk magnetization[27] and resonant X-ray diffraction[28] studies have shown that Néel ordering persists for $x \lesssim 0.17$ and that T_N is monotonically suppressed with x. But no evidence of any broken symmetry phases beyond the Néel phase has been reported in $Sr_2Ir_{1-x}Rh_xO_4$ so far. Remarkably, our SHG measurements show that the hidden phase transition observed in the parent compound also persists on hole doping (Fig. 4b,c) and that, although T_Ω is suppressed with x, the splitting between T_Ω and T_N grows monotonically from approximately 2 K to 75 K between $x = 0$ and $x \sim 0.11$. This provides strong evidence that the Néel and hidden orders are not trivially tied, but are independent and distinct electronic phases.

Our finding of a hidden broken symmetry phase in proximity to an antiferromagnetic Mott insulator reveals a striking parallel between the cuprate and Sr_2IrO_4 phase diagrams (Fig. 4d), which is further strengthened by recent observations of a pseudogap region in $Sr_2Ir_{1-x}Rh_xO_4$ using angle-resolved photoemission spectroscopy[8]. Driving the hidden phase to a quantum critical point[27]

through higher doping may be a route to achieving high-T_c (ref. 12) or parity-odd[29,30] superconductivity in the iridates. Although further theoretical studies are required to establish the microscopic origin of the hidden phase, the fact that it bears the symmetries of a magneto-electric loop-current order already suggests several interesting macroscopic responses, including a linear magneto-electric effect[18] and non-reciprocal optical rotation[17,18].

Methods

Methods and any associated references are available in the online version of the paper.

References

1. Kim, B. J. et al. Novel $J_{eff}=1/2$ Mott state induced by relativistic spin–orbit coupling in Sr_2IrO_4. *Phys. Rev. Lett.* **101,** 076402 (2008).
2. Kim, B. J. et al. Phase-sensitive observation of a spin-orbital Mott state in Sr_2IrO_4. *Science* **323,** 1329–1332 (2009).

3. Dhital, C. *et al.* Neutron scattering study of correlated phase behavior in Sr_2IrO_4. *Phys. Rev. B* **87,** 144405 (2013).
4. Ye, F. *et al.* Magnetic and crystal structures of Sr_2IrO_4: A neutron diffraction study. *Phys. Rev. B* **87,** 140406 (2013).
5. Boseggia, S. *et al.* Locking of iridium magnetic moments to the correlated rotation of oxygen octahedra in Sr_2IrO_4 revealed by X-ray resonant scattering. *J. Phys. Condens. Matter* **25,** 422202 (2013).
6. Torchinsky, D. H. *et al.* Structural distortion induced magneto-elastic locking in Sr_2IrO_4 revealed through nonlinear optical harmonic generation. *Phys. Rev. Lett.* **114,** 096404 (2015).
7. Kim, Y. K. *et al.* Fermi arcs in a doped pseudospin-1/2 Heisenberg antiferromagnet. *Science* **345,** 187–190 (2014).
8. Cao, Y. *et al.* Hallmarks of the Mott-Metal Crossover in the Hole Doped $J = 1/2$ Mott insulator Sr_2IrO_4. Preprint at http://arXiv.org/abs/1406.4978 (2014).
9. De la Torre, A. *et al.* Collapse of the Mott gap and emergence of a nodal liquid in lightly doped Sr_2IrO_4. Preprint at http://arXiv.org/abs/1506.00616 (2015).
10. Kim, Y. K., Sung, N. H., Denlinger, J. D. & Kim, B. J. Observation of a d-wave gap in electron-doped Sr_2IrO_4. Preprint at http://arXiv.org/abs/1506.06639 (2015).
11. Yan, Y. J. *et al.* Signature of high temperature superconductivity in electron doped Sr_2IrO_4. Preprint at http://arXiv.org/abs/1506.06557 (2015).
12. Wang, F. & Senthil, T. Twisted Hubbard model for Sr_2IrO_4: Magnetism and possible high temperature superconductivity. *Phys. Rev. Lett.* **106,** 136402 (2011).
13. Keimer, B., Kivelson, S. A., Norman, M. R., Uchida, S. & Zaanen, J. From quantum matter to high-temperature superconductivity in copper oxides. *Nature* **518,** 179–186 (2015).
14. Varma, C. M. Non-Fermi-liquid states and pairing instability of a general model of copper oxide metals. *Phys. Rev. B* **55,** 14554–14580 (1997).
15. Weber, C., Läuchli, A., Mila, F. & Giamarchi, T. Orbital currents in extended Hubbard models of high-T_c cuprate superconductors. *Phys. Rev. Lett.* **102,** 017005 (2009).
16. Kung, Y. F. *et al.* Numerical exploration of spontaneous broken symmetries in multiorbital Hubbard models. *Phys. Rev. B* **90,** 224507 (2014).
17. Orenstein, J. Optical nonreciprocity in magnetic structures related to high-T_c superconductors. *Phys. Rev. Lett.* **107,** 067002 (2011).
18. Yakovenko, V. M. Tilted loop currents in cuprate superconductors. *Physica B* **460,** 159–164 (2015).
19. Fiebig, M., Pavlov, V. V. & Pisarev, R. V. Second-harmonic generation as a tool for studying electronic and magnetic structures of crystals: Review. *J. Opt. Soc. Am. B* **22,** 96–118 (2005).
20. Simon, M. E. & Varma, C. M. Symmetry considerations for the detection of second-harmonic generation in cuprates in the pseudogap phase. *Phys. Rev. B* **67,** 054511 (2003).
21. Chikara, S. *et al.* Giant magnetoelectric effect in the $J_{eff} = 1/2$ Mott insulator Sr_2IrO_4. *Phys. Rev. B* **80,** 140407 (2009).
22. Ganguly, S., Granas, O. & Nordstrom, L. Non-trivial order parameter in Sr_2IrO_4. *Phys. Rev. B* **91,** 020404(R) (2015).
23. Lovesey, S. W. & Khalyavin, D. D. Strange magnetic multipoles and neutron diffraction by an iridate perovskite (Sr_2IrO_4). *J. Phys. Condens. Matter* **26,** 322201 (2014).
24. Fischer, M. H. & Kim, E.-A. Mean-field analysis of intra-unit-cell order in the Emery model of the CuO_2 plane. *Phys. Rev. B* **84,** 144502 (2011).
25. Scagnoli, V. *et al.* Observation of orbital currents in CuO. *Science* **332,** 696–698 (2011).
26. Di Matteo, S. & Norman, M. R. Orbital currents, anapoles, and magnetic quadrupoles in CuO. *Phys. Rev. B* **85,** 235143 (2012).
27. Qi, T. F. *et al.* Spin–orbit tuned metal-insulator transitions in single-crystal $Sr_2Ir_{1-x}Rh_xO_4$ ($0 \leq x \leq 1$). *Phys. Rev. B* **86,** 125105 (2012).
28. Clancy, J. P. *et al.* Dilute magnetism and spin-orbital percolation effects in $Sr_2Ir_{1-x}Rh_xO_4$. *Phys. Rev. B* **89,** 054409 (2014).
29. Watanabe, H., Shirakawa, T. & Yunoki, S. Monte Carlo study of an unconventional superconducting phase in iridium oxide $J_{eff} = 1/2$ Mott insulators induced by carrier doping. *Phys. Rev. Lett.* **110,** 027002 (2013).
30. Meng, Z. Y., Kim, Y. B. & Kee, H.-Y. Odd-parity triplet superconducting phase in multiorbital materials with a strong spin–orbit coupling: Application to doped Sr_2IrO_4. *Phys. Rev. Lett.* **113,** 177003 (2014).

Author contributions

L.Z. and D.H. planned the experiment. L.Z., D.H.T., H.C. and V.I. performed the measurements. L.Z. and R.L. performed the magnetic point group symmetry analysis. R.F. performed the Landau free energy calculation. T.Q. and G.C. prepared and characterized the samples. L.Z., R.F. and D.H. analysed the data and wrote the manuscript.

Additional information

Supplementary information is available in the online version of the paper. Reprints and permissions information is available online at www.nature.com/reprints. Correspondence and requests for materials should be addressed to D.H.

Competing financial interests

The authors declare no competing financial interests.

Methods

Material growth. Single crystals of Sr_2IrO_4 and $Sr_2Ir_{1-x}Rh_xO_4$ were grown using a self flux technique from off-stoichiometric quantities of IrO_2, $SrCO_3$ and $SrCl_2$ or RhO_2, IrO_2, $SrCO_3$ and $SrCl_2$ respectively. The ground mixtures of powders were melted at $1,470\,°C$ in partially capped platinum crucibles. The soaking phase of the synthesis lasted for $>20\,h$ and was followed by a slow cooling at $2\,°C\,h^{-1}$ to reach $1,400\,°C$. From this point the crucible is brought to room temperature through a rapid cooling at a rate of $100\,°C\,h^{-1}$. The Rh concentration was determined by energy-dispersive X-ray spectroscopy.

RA-SHG measurements. Ultrashort optical pulses with 35 fs duration and 800 nm centre wavelength were produced at a 10 kHz repetition rate from a regeneratively amplified Ti:sapphire laser (KMLabs-Wyvern). The RA-SHG measurements were performed by means of a rotating scattering plane technique[31] using an SHG wavelength $\lambda = 400\,nm$ that is resonant with the O 2p to $J_{eff} = 1/2$ upper Hubbard band transition[32]. Light was obliquely incident onto the sample at a $30°$ angle of incidence with a fluence that was maintained below $1\,mJ\,cm^{-2}$, which is well below the damage threshold of Sr_2IrO_4. Reflected SHG light was collected using a photomultiplier tube. Samples were cleaved either in air or in a nitrogen-purged environment and immediately pumped down to a pressure $<5 \times 10^{-6}$ torr in an optical cryostat. Crystals were oriented before measurement using X-ray Laue diffraction.

SHG microscopy measurements. Wide-field SHG images with a spatial resolution of $\sim 1\,\mu m$ were collected using the same light source as that used for the RA-SHG measurements. A $40°$ oblique angle of incidence was used and the incident light fluence was maintained below $1\,mJ\,cm^{-2}$. The reflected SHG light was collected by an objective lens and focused onto an electron-multiplying charge-coupled device (CCD) camera.

Fitting procedure. The low-($T < T_\Omega$) and high-temperature ($T > T_\Omega$) RA-SHG data were fitted to the expressions $I(2\omega, \varphi) = |A\hat{e}_i(2\omega)\chi^{EQ}_{ijkl}(\varphi)\hat{e}_j(\omega)\partial_k\hat{e}_l(\omega) + A\hat{e}_i(2\omega)\chi^{ED}_{ijk}(\varphi)\hat{e}_j(\omega)\hat{e}_k(\omega)|^2 I(\omega)^2$ and $I(2\omega, \varphi) = |A\hat{e}_i(2\omega)\chi^{EQ}_{ijkl}(\varphi)\hat{e}_j(\omega)\partial_k\hat{e}_l(\omega)|^2 I(\omega)^2$ respectively, where A is a constant determined by the experimental geometry, $I(\omega)$ is the intensity of the incident beam, $\hat{e}$ is the polarization of the incoming fundamental or outgoing SHG light and $\chi^{EQ}_{ijkl}(\varphi)$ and $\chi^{ED}_{ijk}(\varphi)$ are the bulk electric-quadrupole and electric-dipole susceptibility tensors, respectively, transformed into the rotated frame of the scattering plane. The non-zero independent elements of the tensors in the unrotated frame of the crystal are deduced by applying the appropriate point group ($4/m$ for χ^{EQ}_{ijkl} and $2'/m$ or $m1'$ for χ^{ED}_{ijk}) and degenerate SHG permutation symmetries. This reduces χ^{EQ}_{ijkl} to 17 non-zero independent elements ($xxxx = yyyy$; $zzzz$; $zzxx = zzyy = zxxz = zyyz$; $xyzz = -yxzz$; $xxyy = yyxx = xyyx = yxxy$; $xxxy = -yyyx = xyxx = -yxyy$; $xxzz = yyzz$; $zzxy = -zzyx = -zxyz = zyxz$; $xyxy = yxyx$; $xxyx = -yyxy$; $zxzx = zyzy$; $xzyz = -yzxz$; $xzxz = yzyz$; $zxzy = -zyzx$; $yxxx = -xyyy$; $xzzx = yzzy$; $xzzy = -yzzx$) and reduces χ^{ED}_{ijk} to 10 non-zero independent elements (xxx; $xyx = xxy$; xyy; xzz; yxx; $yyx = yxy$; yyy; yzz; $zzx = zxz$; $zzy = zyz$).

References

31. Torchinsky, D. H., Chu, H., Qi, T., Cao, G. & Hsieh, D. A low temperature nonlinear optical rotational anisotropy spectrometer for the determination of crystallographic and electronic symmetries. *Rev. Sci. Instrum.* **85,** 083102 (2014).
32. Moon, S. J. *et al.* Electronic structures of layered perovskite Sr_2MO_4 (M = Ru, Rh, and Ir). *Phys. Rev. B* **74,** 113104 (2006).